Helmholtz-Zentrum Dresden-Rossendorf (HZDR)

HZDR
HELMHOLTZ ZENTRUM
DRESDEN ROSSENDORF

Functionalized silicon substrates with stripe-patterned surface-near electrostatic forces for the self-organized, stable immobilization of biomolecules

Blaschke, D.; Pahlow, S.; Fremberg, T.; Weber, K.; Müller, A. D.; Kurz, S.; Spohn, J.; Dhandapani, V.; Rebohle, L.; Skorupa, I.; Schmidt, H.;

Originally published:

April 2021

Applied Surface Science 545(2021), 148729

DOI: https://doi.org/10.1016/j.apsusc.2020.148729

Perma-Link to Publication Repository of HZDR:

https://www.hzdr.de/publications/Publ-31972

Release of the secondary publication
on the basis of the German Copyright Law § 38 Section 4.

CC BY-NC-ND

Functionalized silicon substrates with stripe-patterned surface-near electrostatic forces for the self-organized, stable immobilization of biomolecules

D. Blaschke[a,b], S. Pahlow[a], T. Fremberg[a], K. Weber[a], A. D. Müller[c], S. Kurz[d], J. Spohn[d], V. Dhandapani[d], L. Rebohle[b], I. Skorupa[b], H. Schmidt[a,e]

[a] *Leibniz Institute of Photonic Technology, Albert-Einstein-Straße 9, 07745 Jena, Germany*
[b] *Institute of Ion Beam Physics and Materials Research, Helmholtz-Zentrum Dresden – Rossendorf, Bautzner Landstraße 400, 01328 Dresden, Germany*
[c] *Anfatec Instruments AG, Melanchthonstraße. 28, 08606 Oelsnitz, Germany*
[d] *Fraunhofer Institute for Ceramic Technologies and Systems IKTS, Perlickstraße. 1, 04103 Leipzig, Germany*
[e] *Friedrich Schiller University Jena, Institute for Solid State Physics, Helmholtzweg 3, 07743 Jena, Germany*

Abstract

Silicon substrates with stripe-patterned surface-near electrostatic forces (SNEF) were prepared by local implantation of boron ions into n-type silicon wafers and of phosphorus ions into p-type silicon wafers in a stripe pattern of 12 µm periodicity. The dependence of SNEF on the concentration of implanted ions, post-annealing conditions, and generation of charge carriers under illumination was investigated by measuring the 1st and 2nd harmonics of the SNEF in the dark and under illumination using Kelvin probe force microscopy. The self-organized immobilization of biomolecules on silicon regions with positive charges occupying the interface states between the silicon and the native SiO_2 has been demonstrated for the negatively charged single stranded deoxyribonucleic acid (DNA) and bovine serum albumin (BSA) proteins.

Keywords: surface-near electrostatic forces, Kelvin probe force microscopy, Si pn-junction, self-organized molecular immobilization, deoxyribonucleic acid, bovine serum albumin

1. Introduction

The immobilization of nano- and micromolecules on solid surfaces plays a crucial role in chemistry, biology, and material science. For example, peptide coatings on dental implants are used to prevent peri-implantitis [1] or enzymatic coatings on nanoparticles are used as coloidal biocatalysts for polymerization reactions [2], or nucleic acid coatings are used to detect single nucleotide polymorphisms [3]. Beside chemical bindings, also an electrostatic potential difference between a surface and electrically charged/polarizable molecules or nanoparticles can be used for surface coating if the surface-near electrostatic force (SNEF) is attractive. For example, one established approach for coating a working electrode with DNA probe monolayers is the use of electrostatic forces between the negatively charged phosphate groups of DNAs and the positive charges of the working electrode. However, the DNA probe monolayers are immobilized in a random orientation at multiple sites of the working electrode and are in a high risk in terms of desorption from the working electrode under the influence of pH buffer, ionic strength, and temperature [4].

Here we use silicon with an ion implanted electrostatic charge pattern (PolCarr substrates). Without further treatment a native, approximately 1–2 nm thin SiO_2 layer forms on the Si surface. Subsequently, immobile interface charges which are independent of the pH buffer occupy interface states at the interface between the native SiO_2 and the implanted silicon. The areal density of the immobile interface charges amounts to $10^{12}\,cm^{-2}$ and is more than four orders of magnitudes larger than the areal density of the mobile and pH buffer dependent surface charges. Therefore, PolCarr substrates are stable in time as correlated to the envisaged self-organized immobilization of biomolecules. Ion implantation was developed as a method of producing pn-junctions in silicon photovoltaic devices in the late 1970s and has been used in this work to fabricate stripe-patterned SNEF with a periodicity of 12 µm. Because of its up-scalability, ion implantation technology may be used to fabricate planar silicon with electrostatic charge pattern on the wafer level with pattern sizes down to few micrometers and few nanometers if photolithography and electron beam lithography is used for writing the ion implantation mask, respectively. Because of the immobile interface charges the electrostatic charge pattern of the PolCarr substrates is present without application of a bias and does allow for a self-organized immobilization of charged analytes by electrostatic forces [5] which is of po-

*Corresponding authors.
Email addresses: daniel.blaschke@leibniz-ipht.de (), heidemarie.schmidt@leibniz-ipht.de ()

tential use in biotechnology, biochemistry, and biophysics. In this work the stripe-patterned SNEF of PolCarr substrates have been characterized by Kelvin probe force microscopy (KPFM) measurements in the dark and under illumination. KPFM is a scanning probe force microscopy technique which was developed in 1991 by Nonnenmacher et al. [6] by combining atomic force microscopy (AFM) with the Kelvin method, invented by Lord Kelvin in 1898 [7]. Nowadays, KPFM is a well established method, e.g. for the quantitative dopant profiling of semiconductors by determining the energetic position of the Fermi level [8, 9] or for the estimation of the minority carrier diffusion length by measuring the surface photovoltage between an AFM tip and the sample surface [10]. Furthermore, KPFM can be used for the characterization of the interaction strength between a surface and its environment on the micrometer to nanometer length scale by determining the surface potential. We have modelled the SNEF in the dark with the Baumgart-Helm-Schmidt (BHS) model [8] and with the corrected contact potential difference (CPD) model [11].
As an example, in this work we show the self-organized immobilization of deoxyribonucleic acid (DNA) single strands and bovine serum albumin (BSA) in solutions with a pH of 7 on PolCarr substrates. Due to the negative charge of DNA and BSA, the local immobilization on PolCarr substrates is always observed at boron doped regions with positively charged defects in the SiO_2/Si interface as a result of the attractive electrostatic forces.
In a recent work, Jo et al. have shown the immobilization of thiol-modified complementary DNA on nanoporous gold thin film electrodes using electrostatic binding to detect H_2O_2 with electrochemical signal enhancement and high selectivity [12]. Furthermore, also using electrostatic binding, Jia et al. showed the immobilization of BSA on SiO_2 nanoparticles in a silane-coupling ion liquid [13] which is of importance for protein purification and a wide range of applications, including biosensors, biocatalysis, and biomedical devices [14].

2. Material and methods

2.1. Preparation of PolCarr substrates

PolCarr (short form of **Pol**arized **Carr**ier) substrates were prepared by using n- and p-doped 4 inch ⟨100⟩-Si wafers with a specific resistivity of 1–5 Ω×cm, which corresponds to a dopant concentration of $(1–5)\times10^{15}$ P/cm^3 and $(3–15)\times10^{15}$ B/cm^3, respectively. Prior to the implantation, the wafers underwent RCA cleaning to remove organic and ionic contaminations, and a 1 µm thick SiO_2 layer was formed on top by wet chemical oxidation to smear out the depth profile of implanted ions. The mask used for the implantation of B ions into Si:P wafers and of P ions into Si:B wafers was realized using a stripe-patterned resist with a periodicity of 12 µm and 2 µm wide stripes without resist, pitched by 10 µm wide stripes with resist. After removing the resist mask, some PolCarr substrates were annealed in a furnace under nitrogen atmosphere for 1 h at 900 °C. Finally, the SiO_2 layer was removed by HF and the 4 inch wafers B1, B2, P1, and P2 were cut into 1×1 cm^2 sample pieces.
The parameters for the ion implantations are given in Tab. 1. Corresponding dopant profiles in Si, simulated with SRIM [15], are shown in Fig. 1.

Table 1: Species, fluence, and energy of implanted boron (B) ions in silicon wafers with host crystal dopant concentration of $(1-5) \times 10^{15}$ P/cm^3 and phosphorus (P) ions into silicon wafers with host crystal dopant concentration of $(3-15) \times 10^{15}$ B/cm^3.

Sample	Ion	Fluence (ions/cm^2)	Energy (keV)
B1	B	3×10^{13}	450
B2	B	8×10^{15}	400
P1	P	3×10^{13}	1000
P2	P	3×10^{15}	1000

2.2. AFM/KPFM measurements

Surface potentials were characterized by KPFM using an Anfatec Level-AFM under nitrogen atmosphere, and Pt coated n-type Si cantilevers (MikroMasch HQ:NSC18/Pt, $f_{\mathrm{res}} = 75$ kHz, $k = 2.8$ N/m) with a typical tip radius of less than 30 nm.
During KPFM measurements topography and electrical signals were probed simultaneously in amplitude modulation mode. The 1st eigenmode and 2nd eigenmode of the cantilever lies at a frequency of about 75 kHz and of 450 kHz, respectively. The 1st harmonic of the 1st eigenmode was used to detect the topography and 1st and 2nd harmonics of the 2nd eigenmode was used to probe the surface potential and the free carrier concentration, respectively.
For quantitative measurements, the contribution from the interaction between the cantilever and the sample area was taken into account by retracting the tip to a distance of (1-3 µm) with switched off Kelvin feedback. The remaining electrical signal was used as an offset compensation in the Anfatec software. This approach is explained in detail in Ref. [16].
The KPFM measurements of the Si samples were performed in the dark and under illumination from a green LED inside the AFM head. In order to prevent unwanted photo-generated charge carriers during the dark measurements, an IR laser with a wavelength of 1500 nm was used to detect the deflection of the AFM tip. In addition, the whole AFM system was operated under an opaque cover. Furthermore, the influence of photo-generated charge carriers to the KPFM signal was characterized by using the green LED.

2.3. Handling of DNA single strands

A 30mer oligonucleotide (5'-TTTTTTCAGCATGTGC-TCCTTGATTCTATG-3') with a biotin-tetra(ethylene gly-

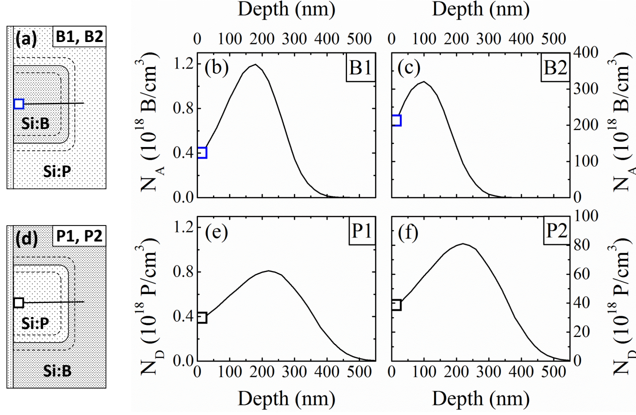

Figure 1: Schematic cross-sectional view on (a) Si:P PolCarr substrates implanted with boron ions and (d) Si:B PolCarr substrates implanted with phosphorus ions showing the implanted regions and the extension (not to scale) of the space charge regions (scattered lines). The solid line in (a) and (d) runs through an implanted region, i.e. through a stripe with 2 µm nominal width, and ends at a depth of about 550 nm. Simulated acceptor concentration N_A and donor concentration N_D using SRIM [15] according to the implantation parameters are given in Tab. 1 of the (b,c) Si:P PolCarr substrates implanted with boron ions and (e,f) Si:B PolCarr substrates implanted with phosphorus ions, respectively. The depth 0 nm is marked with blue (a-c) and black (d-f) symbols and represents the position where dopant concentration has been used to determine the Fermi level (Fig. 4).

col) label at the 3'-end and a (6-Amino)hexyl function at the 5'-end was diluted to a final concentration of 50 µM with 1x Array-it micro spotting solution (Array-it Corporation, USA). Spots with a volume of 1 µl were manually applied onto the substrate surface using a micropipette. The substrates were incubated overnight at room temperature in a humidity chamber to prevent the droplets from drying. Subsequently, the substrates were immersed in 1x phosphate buffered saline (1x PBS: 137 mM NaCl, 2.7 mM KCl, 4.3 mM Na_2HPO_4, 1.4 mM KH_2PO_4, pH 7.4) and washed for 30 s using a swiveling table. Following this, $1 \times 1\,\mathrm{cm}^2$ large pieces of PolCarr substrates were dried using pressurized air and then coated with 80 µl per chip of a 1:1000 dilution of streptavidin conjugated horseradish peroxidase (Sigma-Aldrich, Germany) in 1x PBS with 0.5 % Tween 20 (1x PBST). After a 40 min incubation period at room temperature, the substrates were washed three times for 1 min with 1x PBST and then rinsed two times with deionized water. Finally, the enzyme catalyzed silver deposition was performed using the EnzMet® kit (Nanoprobes Inc., USA) according to the manufacturer's protocol.

2.4. Handling of bovine serum albumin

$1 \times 1\,\mathrm{cm}^2$ large pieces of PolCarr substrates were put in a 24-well-plate and equilibrated in steril 1x PBS for 15 min at room temperature. PBS was removed and 750 µg/cm^2 bovine serum albumin (BSA) (Sigma-Aldrich, Germany) reconstituted in 1x PBS (3 mg/ml) was added to the substrates. The substrates were incubated at 37 °C for 24 h to attach the BSA to the substrate surface. Excess BSA was removed by washing the samples once with 1x PBS. Before labelling the BSA with primary (anti-BSA antibody 1:500 (Thermo Scientific, Cat # A11133)) and secondary antibody (Alexa Fluor 488 donkey anti-rabbit antibody 1:500 (Dianova, Cat # 711-545-152)), the Si surface was blocked with 750 µg/cm^2 human fibrinogen (Sigma-Aldrich, Germany) reconstituted in 0.9 % NaCl (3 mg/ml) for 30 min. Primary antibody in fibrinogen blocking solution was added and incubated for 1 h at room temperature. After three washing steps with 1x PBS the secondary antibody in fibrinogen blocking solution was added and incubated for 1 h at room temperature in the dark followed by three times washing with 1x PBS. At the end, the substrates were covered with immunoselect anti fading mounting medium (Dianova, Germany) and images were taken with confocal microscope. Secondary antibody controls showed no unwanted adsorption on the substrates.

3. Theory

3.1. Physical background of KPFM measurements

Kelvin probe force microscopy (KPFM) is a special tapping mode AFM technique where the electrostatic force between a conductive tip and the sample surface is measured by amplitude or frequency modulation. The electrostatic force of the tip-sample system is given by [16]:

$$F = \frac{1}{2}\frac{\partial C}{\partial z}U^2 \ , \tag{1}$$

where C is the tip-sample capacitance, z the tip-sample distance and U a bias voltage. The bias voltage U is the sum of the voltage U_s applied to the sample and of the sample-system bias U_{ss}, which depends on tip and sample material. The voltage U_s consists of a dc part U_{dc} and an ac part with amplitude U_{ac} and frequency f. Therefore, U is written as follows:

$$U = U_s + U_{ss} = U_{dc} + U_{ac}\sin(2\pi f t) + U_{ss} \ . \tag{2}$$

Substituting Eq. (2) in Eq. (1) yields the electrostatic force acting onto the AFM tip:

$$F = \frac{1}{2}\frac{\partial C}{\partial z}\left[(U_{dc} + U_{ss}) + U_{ac}\sin(2\pi f t)\right]^2 \ . \tag{3}$$

This equation can be separated into a static and two frequency dependent forces:

$$F_{dc} = \frac{\partial C}{\partial z}\left[\frac{1}{2}(U_{dc} + U_{ss})^2 + \frac{U_{ac}^2}{4}\right] \ , \tag{4}$$

$$F_f = \frac{\partial C}{\partial z}(U_{dc} + U_{ss})\,U_{ac}\sin(2\pi f t) \ , \tag{5}$$

$$F_{2f} = -\frac{\partial C}{\partial z}\frac{1}{4}U_{ac}^2\left[\cos(2\pi 2 f t)\right] \ . \tag{6}$$

The 2nd harmonic force F_{2f} acting on the AFM tip can be used to determine the dopant concentration in the semiconductor via its dependence on the capacitance gradient $\partial C/\partial z$. A first order approximation of the tip-sample capacitance C might be given by the insulator capacitance of the gap between tip and sample surface C_i in series with the capacitance C_d of the depletion layer inside the semiconductor:

$$C = \frac{C_i C_d}{C_i + C_d} \ . \tag{7}$$

The capacitance of a depletion layer inside a semiconductor is proportional to the square root of the relative permittivity of the semiconductor ϵ_s and the doping concentration N which equals free carrier concentration if all dopants are ionized:

$$C_d \propto \sqrt{\epsilon_s N} \ . \tag{8}$$

Substituting Eq. (8) into Eq. (7) and assuming a depth independent doping concentration N, the derivation of the capacitance is described by:

$$\frac{\partial C}{\partial z} \propto \frac{\epsilon_s N}{(C_d + C_i)^2} \frac{\partial C_i}{\partial z} \ . \tag{9}$$

For $C_i \gg C_d$, Eq. (9) simplifies to:

$$\frac{\partial C}{\partial z} \propto \frac{\epsilon_s N}{C_i^2} \frac{\partial C_i}{\partial z} \ . \tag{10}$$

Eq. (10) and Eq. (6) show the linear dependence of data measured on the 2nd harmonic F_{2f} to the doping concentration N. However, experimentally the influence on N is less pronounced due to similar magnitudes of C_i and C_d, but still present.

The 1st harmonic force F_f [Eq. (5)] acting on the AFM tip is used for the measurement of the sample system bias U_{ss} (also called Kelvin bias) by setting the term $(U_{dc} + U_{ss})$ to the compensation offset value using the Kelvin feedback loop.
The interpretation of the Kelvin bias measured on doped silicon with flat surfaces and a native SiO_2 is still being discussed. To remove all dopant-independent contributions to the Kelvin bias, a viable option is the discussion of the Kelvin bias variation ΔU_K between differently doped regions of silicon. In the following we present the two main ΔU_K models discussed in literature.

3.2. BHS model

One model explaining the variation of Kelvin bias measured on doped silicon with different dopant concentrations, the BHS model, was derived by Baumgart, Helm, and Schmidt [8]. The BHS model proposes that the electrostatic force between the tip on the vertically oscillating AFM cantilever and the semiconductor sample has its origin in the asymmetric electric dipole which is formed by the interface states between native SiO_2 and doped silicon and the ionized dopant ions in the surface-near depletion layer. The interface states are occupied by electrons in phosphorus (Si:P) and by holes in boron (Si:B) doped silicon, respectively [Fig. 2(c)]. During KPFM measurements the force to the tip is minimized by applying a bias U_{dc} to the sample in a feedback loop until the electrostatic force does not influence the cantilever oscillations any more. In a semiconductor sample-system this is realized by injecting majority charge carriers into the surface-near depletion layer which screen the ionized dopant ions in the surface-near region. To fulfill the charge neutrality condition, the interface states are discharged simultaneously. According to the BHS model, the measured U_{dc} bias (sum of the Kelvin bias and a correction bias) is correlated with the difference between the Fermi energy E_F(Si:P) or E_F(Si:B) and the respective band edge E_C or E_V for Si:P or Si:B, respectively [Fig. 2(d), Eq. (11), Eq. (12)]:

$$-q \cdot U_K^{BHS}(\text{Si:P}) = E_C - E_F(\text{Si:P}) \ , \tag{11}$$

$$-q \cdot U_K^{BHS}(\text{Si:B}) = E_V - E_F(\text{Si:B}) \ , \tag{12}$$

where q is the charge of an electron.
The Kelvin bias difference ΔU_K^{BHS} is calculated from Eq. (11) and Eq. (12) as follows:

$$\Delta U_K^{BHS} = E_g - E_F(\text{Si:P}) + E_F(\text{Si:B}) \ , \tag{13}$$

where the bandgap $E_g = E_C - E_V$.
In addition, the lateral electric field in the space charge region at the pn-junction partially prevents the injection of majority charge carriers and distorts the expected Kelvin bias.
However, experimentally measured voltages differ typically from the values calculated using Eq. (11) or Eq. (12). This is due to a KPFM correction bias U_{corr} caused by traps in the oxide layer, defects at the SiO_2/Si interface and differences between the work function of the AFM tip and the work function of the silicon. Therefore, the dc voltage U_{dc} applied to the sample for minimizing the electrostatic force between tip and sample surface is the sum of the KPFM correction bias U_{corr} and the Kelvin bias U_K:

$$U_{dc} = U_{corr} + U_K \ . \tag{14}$$

Note that without a correction, the measured dc voltage is equal to the Kelvin bias, which is positive for a Si:P region and negative for a Si:B region.

If a semiconductor is illuminated quasi-Fermi levels $E_{F,n}$(Si:P) and $E_{F,p}$(Si:B) are formed. Because the concentration of majority charge carriers increases under illumination, the quasi-Fermi levels $E_{F,n}$(Si:P) and $E_{F,p}$(Si:B) are shifted closer to the corresponding band edge and one can find the following relation:

$$E_C - E_F(\text{Si:P}) > E_C - E_{F,n}(\text{Si:P}) > 0 \ , \tag{15}$$

$$E_V - E_F(\text{Si:B}) < E_V - E_{F,p}(\text{Si:B}) < 0 \ . \tag{16}$$

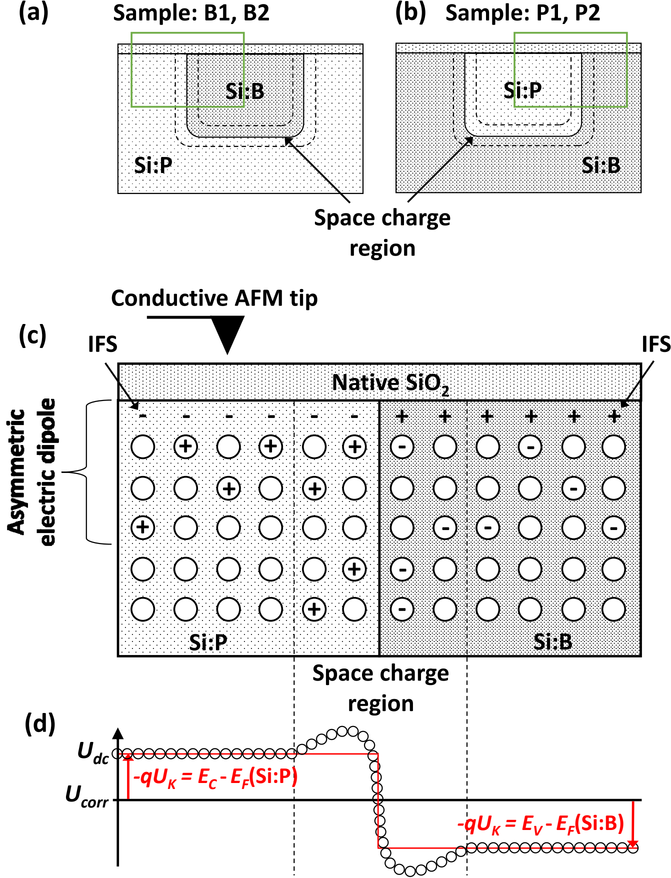

Figure 2: Cross-section of PolCarr substrates for (a) ion implantation of B into a Si:P doped host crystal (sample type B1, B2) and (b) ion implantation of P into a Si:B doped host crystal (sample type P1, P2). The green inset is explained in more detail in (c). (c) Cross-section of surface-near region in Si:P and Si:B with thin native oxide layer. A vertical space charge region is formed at the Si:P/Si:B interface. In addition, an asymmetric electric dipole consisting of mobile charge carriers (-,+) which are trapped in interface states (IFS) and the same amount of ionized dopant atoms is built up near the Si surface. The electrostatic force on the conductive AFM tip is minimized by injection of majority charge carriers into the Si surface region by applying a dc voltage. (d) Sketch of calculated (red line) and of experimentally observed (black open circles) dc voltages U_{dc} applied to a sample with a pn-junction. U_{dc} is shown together with correction bias U_{corr} and Kelvin bias U_K and can be calculated using Eq. (11) and Eq. (12), after Ref. [8].

3.3. CPD model extended to semiconductors with surface charges

The contact potential difference (CPD) model was used by Nonnenmacher et al. [6] in 1991 to explain the data measured on metallic samples by the newly introduced KPFM technique. The model interprets the KPFM data as the contact potential difference i.e. the work function difference between a conductive AFM tip and the metal sample surface. The CPD model was also used on semiconductors later on [17–19].
In the following, the CPD model is explained in more detail using as an example a semiconductor pn-junction, after Ref. [17]. The energetic situation is illustrated in Fig. 3. When the sample is not biased, the Fermi level of the AFM tip and the semiconductor is equal. A contact potential difference between AFM tip with work function Φ_m and the silicon surface with work functions $\Phi(\text{Si:P})$ and $\Phi(\text{Si:B})$ for the P or B doped region of the pn-junction appears. According to the CPD model the electric field due to the work function difference is nullified by applying the Kelvin bias U_K^{CPD} to the sample, which is for the phosphorus doped region given by:

$$q \cdot U_K^{CPD}(\text{Si:P}) = \Phi_m - \Phi(\text{Si:P}) \ , \tag{17}$$

and for the boron doped region given by:

$$q \cdot U_K^{CPD}(\text{Si:B}) = \Phi_m - \Phi(\text{Si:B}) \ . \tag{18}$$

Hence the measured contact potential difference ΔU_K^{CPD} at a pn-junction is:

$$-q \cdot \Delta U_K^{CPD} = E_F(\text{Si:P}) - E_F(\text{Si:B}) \ , \tag{19}$$

which is the same as the built-in potential Φ_b/q if there are no surface charges on the sample. There exist fixed surface charges on the native SiO_2 layer σ_{sf} which are independent on the dopants in silicon and interface charges σ_{ss} occupying the interface states between SiO_2 and silicon. Note that such interface charges [IFS in Fig. 2(c)] and unscreened dopants in a semiconductor form the surface-near, asymmetric electrostatic dipole from which the BHS model starts (Ref. [8]). The altering of the surface potential by interface states and fixed surface charges and interface charges is addressed in detail in Refs. [11, 20] by Polak and Wijngaarden.

3.4. Determination of Fermi energy

In the case of negligible intrinsic conduction i.e. $n_i << N_D, N_A$, which is reasonable in this study because the amount of intrinsic charge carriers in Si is given by 1×10^{10} cm^{-3} at 300 K and if the charge density saturates towards N_D, N_A, which is also true at room temperature for P or B doping in Si, the Fermi level without illumination is approximately given by [22]:

$$E_C - E_F(\text{Si:P}) \cong -kT \ln\left(\frac{N_D}{N_C}\right) \ , \tag{20}$$

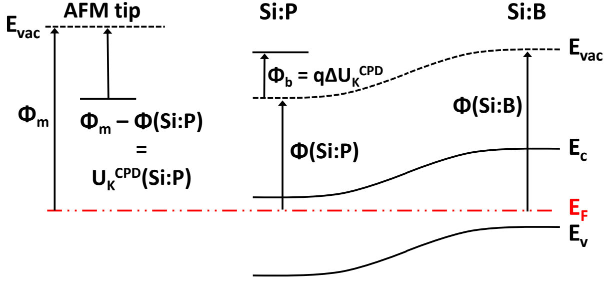

Figure 3: Schematic drawing of the band diagram of a pn-junction measured by KPFM with a metallic AFM tip, after Refs. [17, 21].

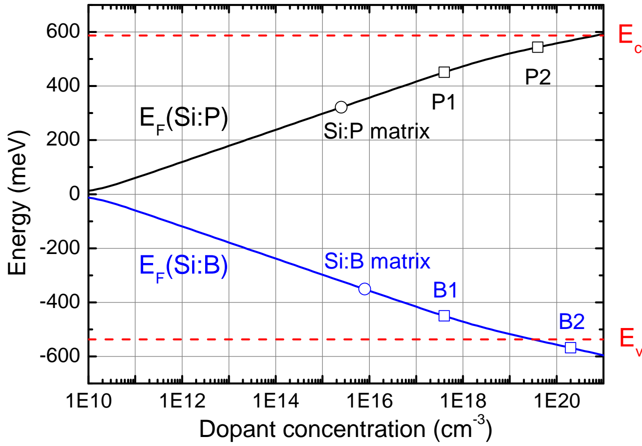

Figure 4: Calculated Fermi energy for P doped Si (black line) and for B doped Si (blue line) in dependence on the doping concentration at 300 K. The intrinsic Fermi level E_i is set to zero. The related positions of the conduction band edge E_c and valence band edge E_v are illustrated by the red dashed lines. It is assumed that E_c and E_v do not depend on the dopant concentration. The squares represent the Fermi level for samples P1, P2, B1 and B2 and the circles show the Fermi level of the Si host material.

$$E_V - E_F(\text{Si:B}) \cong kT \ln\left(\frac{N_A}{N_V}\right) , \quad (21)$$

where N_D, N_A is the doping concentration with P or B, respectively. N_C, N_V describe the conduction band edge density and valence band edge density, respectively. In Si at 300 K N_C amounts to 7.28×10^{19} cm^{-3} and N_V amounts to 1.05×10^{19} cm^{-3}. However, for samples B2 and P2 which were implanted with high fluence (Tab. 1) the Fermi level lies next to the band edges and the above mentioned equations, which are based on the Boltzmann approximation, are not valid. Therefore, the Fermi-Dirac integral has to be numerically solved to obtain the position of the Fermi level. The result is shown in Fig. 4.

4. Results and Discussion

4.1. KPFM in the dark

Fig. 5 shows KPFM measurements on the 1st harmonic [F_f, Eq. (5)], which were done to characterize the electrostatic surface potentials of the PolCarr samples. The measured U_{dc} were corrected by a conveniently chosen correction voltage to facilitate comparison of different samples. For boron implanted stripes in Si:P wafers, U_{dc} is smaller than for the host material, Fig. 5(a,b). In contrast, phosphorus implantation in Si:B wafers leads to a larger U_{dc}, Fig. 5(c,d). This means that phosphorus doped regions show a higher surface potential in comparison to boron doped regions.
Please note that differences in the width of the patterns is caused by variations in the width of stripes without resist during preparation of the implantation mask.
Additionally, at the edges of the implanted stripes a darker or brighter thin stripe is visible for B or P implantation, respectively. These stripes are caused by the space charge region at the pn-junction between implanted regions and the silicon host material.
In order to understand observed differences in electrostatic surface potentials of PolCarr substrates in dependence on ion fluence and post-annealing (Fig. 5), one has to consider the effects caused by ion implantation to the silicon host crystal. Ion implantation in silicon leads to lattice disorder by the introduction of impurities and the generation of intrinsic defects. Accumulation of defects can precede to amorphization of the Si crystal. The simulated concentration of displaced Si atoms using the "Detailed Calculation with full Damage Cascades" mode in SRIM amounts to about 2×10^{21} cm^{-3} (4 % of the Si host crystal) and to about 5×10^{20} cm^{-3} (1 % of the Si host crystal) for P and B implantation with a fluence of 3×10^{13} ions/cm^2, respectively. This means that the irradiation with high fluence (3×10^{15} P/cm^2 or 8×10^{15} B/cm^2) hints to amorphization of the Si host crystal. However, note that SRIM does not take into account different effects during implantation e.g. defect annealing, diffusion of implanted ions, fluence rate effects, and ion channeling. Hence, the simulated defect concentration is typically too large and gives only an upper limit.
The effect of impurities like B or P ions on the conductivity of Si wafers depends on the lattice site and their electronic configuration. Furthermore, also intrinsic defects can be electrically active [23]. It is well known that implanted boron and phosphorus ions in Si can exist at least in three different forms, as substitutional, interstitial or a boron-vacancy or phosphorus-vacancy complex in which the B or P atom is slightly shifted towards the vacancy [24, 25]. Note that only substitutional dopant ions are electrically active and act as shallow acceptors or donors in the case of B or P, respectively. The amount of substitutionals in as-implanted Si is a function of temperature and fluence during ion implantation. Typically, at room temperature several ten percent are substitutionals with a decreasing

tendency for an increasing fluence due to a reduced topological constraint of the silicon crystal with increased radiation damage [23]. An annealing step at 900 °C after ion implantation increases the amount of substitutionals to a value greater than 90% [24, 26]. Furthermore, radiation defects which can compensate free charge carriers are annealed [27] and amorphized layers (high fluence samples B2 and P2) are recrystallized [28].
Hence, the increased contrast between implanted and non-implanted regions after the annealing step in Fig. 5 can be explained with the electrical activation of implanted ions and/or the reduction of charge compensating defects, resulting in a larger doping concentration and a shift of the Fermi energy.
Tab. 2 summarizes the measured Kelvin bias difference ΔU_K between n- and p-doped regions of different samples with and without light illumination. The influence of light is explained later in Sec. 4.3. In addition, the experimentally observed ΔU_K is compared with the theoretical value, which is expected after the Baumgart, Helm, Schmidt (BHS) model ΔU_K^{BHS} [8] and the contact potential difference (CPD) model ΔU_K^{CPD} [6]. Both interpretations of KPFM measurements on semiconductor surfaces are explained in more detail in Sec. 3. It is obvious that the BHS model fits much better to the experimentally observed values in comparison to the CPD model, where the expected values are much too large. Especially in the case of boron doping with post-annealing the values of the BHS model agree very well. However, a disadvantage of the CPD model is that it neglects the band bending at the semiconductor surface due to charged interface and surface states. This issues was addressed by Polak and Wijngaarden [11, 20]. They calculated the band bending at the semiconductor surface and its influence to the CPD model in dependence on the doping concentration of the semiconductor, the concentration of a positive or negative fixed surface charge and the concentration and energetic distribution of interface states. We included the density values, necessary to achieve the experimental measured Kelvin bias difference with the CPD model, for a positive fixed surface charge and for one model of interface states at the SiO_2/Si interface into Tab. 2. The chosen interface states model has Gaussian distributed acceptor and donor states centered at $E_g/2 \pm 0.1$ eV respectively and a standard deviation of 0.04 eV. The density values were taken from the diagrams in Ref. [20]. Both models show reasonable charge density values to adjust the theoretically calculated CPD voltage with the experimental measured one.
By using the Gaussian interface model there might be the trend visible that a higher doping concentration leads to a larger defect density and the post-annealing step reduces the defect density, which seems rational. However, in the case of a positive fixed surface charge this observation is not longer valid for samples P1 and P2.

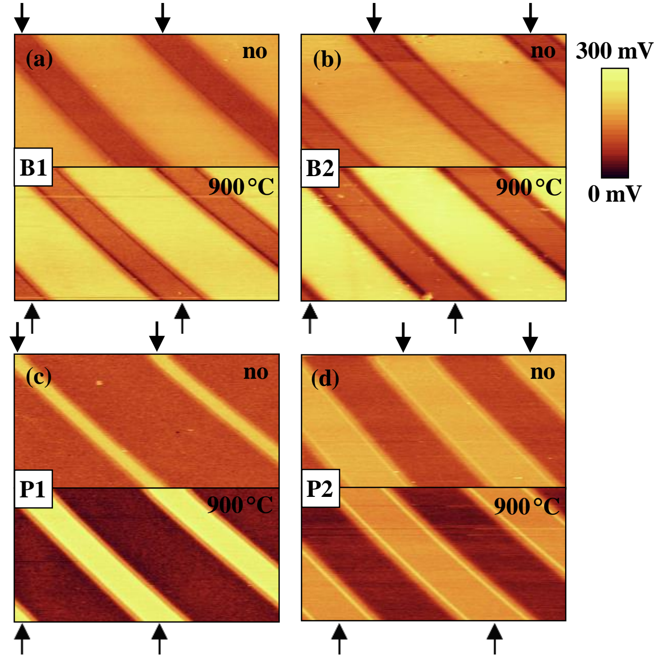

Figure 5: Measured U_{dc}, corrected with a conveniently chosen correction voltage for better comparison of different samples. Measurements were done in the dark at frequency f for boron (a,b) or phosphorus (c,d) implanted Si samples. The arrows indicate implanted stripe-like regions and the fast scan axis had an angle of 45° with respect to the implanted stripe-like pattern. Note that the topography images (not shown here) are flat and do not follow the stripe-like pattern of measured U_{dc}.

4.2. 2nd harmonic measurements in the dark

Measurements on PolCarr substrates on the 2nd harmonic (F_{2f}) are shown in Fig. 6. These measurements were done without Kelvin feedback, i.e. $U_{dc} = 0$. The signal variation can be related with a variation in $\partial C/\partial z$ [Eq. (6)], which gives an information about the amount of free charge carriers which can follow the applied test voltage with amplitude U_{ac} and frequency f. As expected the thick bright stripes in Fig. 6 correspond to the ion implanted areas with a large concentration of free charge carriers. Additionally, the annealed PolCarr substrates (900 °C in Fig. 6) show on both sides of the thick bright stripes a thin bright stripe, separated by a darker line of the same colour as the non-implanted material. This thin line confirms the depletion of free charge carriers from the space charge region between implanted stripes and non-implanted host crystal. Because free charge carriers are smeared out over the Debye length at the end of the space charge region, the thin bright stripes on both sides of the thick bright stripes are detected [8]. The Debye length is calculated to be about 80 nm and 40 nm in the phosphorus doped and boron doped Si host crystal, respectively.
As already observed for measurements on the 1st harmonic (Fig. 5), the annealing step increases also the contrast between implanted and non-implanted regions for measurements on the 2nd harmonic, which is the result of an increased amount of free charge carriers caused by the elec-

Table 2: Experimental ΔU_K and calculated ΔU_K^{BHS} and ΔU_K^{CPD} Kelvin bias difference determined between implanted and non-implanted regions of the samples B1, B2, P1, and P2 in the dark (no) and under illumination (yes). The correction bias U_{corr} has been applied to the whole line scan (B1, B2 in Fig. 7 and P1, P2 in Fig. 8) and is set to zero at the position of the non-implanted regions of the Si:P host crystal and Si:B host crystal with $(1-5)\times 10^{15}$ P/cm^3 and with $(3-15)\times 10^{15}$ B/cm^3, respectively. The modelled Kelvin bias difference ΔU_K^{BHS} (Ref. [9]) and ΔU_K^{CPD} (Ref. [17]) has been calculated using Eqs. (13) and (19), respectively. Furthermore, the interface charges σ_{ss}^{Gauss} and fixed surface charges σ_{sf}, necessary to equal ΔU_K^{CPD} with ΔU_K experimental are given.

Sample	Illum.	U_{corr} (mV)	ΔU_K (mV) experimental	ΔU_K^{BHS} (mV) calculated	ΔU_K^{CPD} (mV) calculated	σ_{ss}^{Gauss}/e (cm^{-2})	σ_{sf}/e (cm^{-2})
B1 no	no	350	115	335	772	$10^{12}-10^{13}$	$10^{12}-10^{13}$
	yes	350	90				
B1 900 °C	no	-335	375	335	772	$10^{11}-10^{12}$	$10^{11}-10^{12}$
	yes	-335	435				
B2 no	no	100	240	250	890	$10^{13}-10^{14}$	$10^{13}-10^{14}$
	yes	100	230				
B2 900 °C	no	330	240	250	890	$10^{13}-10^{14}$	$10^{13}-10^{14}$
	yes	330	280				
P1 no	no	520	120	315	802	$10^{12}-10^{13}$	$10^{12}-10^{13}$
	yes	520	45				
P1 900 °C	no	560	230	315	802	$10^{11}-10^{12}$	$10^{12}-10^{13}$
	yes	560	235				
P2 no	no	470	95	225	895	$10^{13}-10^{14}$	$10^{11}-10^{12}$
	yes	470	55				
P2 900 °C	no	350	130	225	895	$10^{13}-10^{14}$	$10^{11}-10^{12}$
	yes	350	170				

trical activation of implanted ions. In addition, the samples implanted with the large fluence (B2 and P2) show also an increased contrast in comparison to the low fluence samples (B1 and P1) due to the higher doping level.

4.3. KPFM under illumination

Illuminating silicon with only a native SiO_2 layer with visible light results in the generation of electron-hole pairs in the surface-near region. Due to the exponential decrease of light intensity with increasing penetration depth, also the number of photo-generated electron-hole pairs decreases with increasing penetration depth. As a result the distribution of free charges is mainly in the surface-near region. Consequently change of the surface potential is observed which will change the asymmetric, electrostatic dipole (Fig. 2). The measured Kelvin signal is shown in Fig. 7 for B implanted Si:P and in Fig. 8 for P implanted Si:B substrates. For an easier comparison of the different samples, the measured Kelvin bias in the dark on non-implanted regions is corrected by an offset value U_{corr} to set it to zero. Same U_{corr} has been applied to the measured Kelvin bias under illumination. U_{corr} is given in Tab. 2. The following three main observations were made:

1. Illumination of the Si substrates leads to a shift towards smaller/larger Kelvin bias for boron/phosphorus doped substrates, independently from the ion implantation.
2. The Kelvin bias overshoot at the pn-junction which is visible in the dark is no longer observable under illumination.
3. Under illumination the shift of the Kelvin signal is stronger/smaller for non-implanted host wafers than the shift of the Kelvin bias on implanted stripes in non-annealed samples/annealed samples.

These observations can be explained with the surface photovoltage effect [29, 30], describing the formation of a surface voltage i.e. the change of the surface potential, if photo-generated charge carriers are redistributed. The redistribution of charge carriers in a semiconductor is driven because of diffusion as a result of a concentration gradient, drift due to an external applied voltage or drift due to a so called built-in voltage as a result of separated charges in the semiconductor. In the PolCarr samples (Fig. 2), two locations of charge separation exist. This is on the one hand at the SiO_2/Si interface and on the other hand at the pn-junction formed as a result of the ion implantation. At the SiO_2/Si interface the bands in a n/p-type silicon are bend upwards/downwards resulting in a drift of excess electrons/holes away from the surface. Therefore, the density of surface trapped electrons/holes is reduced and decreases the band bending. This results in a positive/negative surface voltage for n/p-type silicon, respectively. Note that for the Kelvin bias the sign convention is opposite. Hence the shift to smaller/larger measured Kelvin bias with illumination is explained in case of the non-implanted regions of samples B1 and B2 (Fig. 7, phosphorus doped Si host matrix) and samples P1 and P2 (Fig. 8, boron doped Si host matrix), respectively. Based on this explanation, the implanted regions should show a shift in the opposite direction as observed. The reason

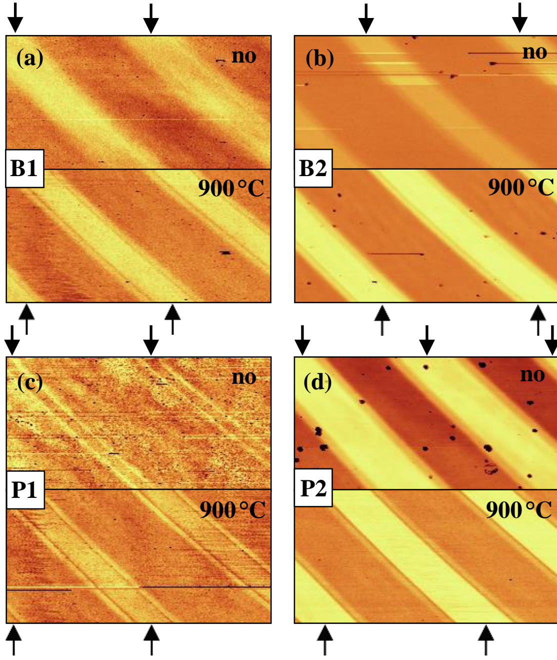

Figure 6: $\partial C/\partial z$ dependence, measured in the dark at frequency $2f$ for boron (a,b) or phosphorus (c,d) implanted Si samples. The arrows indicate implanted stripe-like regions and the fast scan axis had an angle of 45° with respect to the implanted stripe-like pattern. Note that the topography images (not shown here) are flat and do not follow the stripe-like pattern of measured $\partial C/\partial z$.

why this was not seen has its origin at the pn-junction, where also charge separation of photo-generated carriers takes place. Electrons drift from the p-side to the n-side and holes the other way around. This means for the PolCarr samples that in the implanted regions, two competing photo-generated currents exist. To fulfil point 1 of our observation, we can conclude that the photo-generated current of the pn-junction dominates the photo-generated current of the SiO_2/Si interface.
An explanation for point 2 might be that under illumination the built-in voltage of the space charge region is decreased and also its width, which results in a smaller disturbance of the necessary Kelvin bias to nullify the force between AFM tip and sample surface.
Point 3 can be explained as follows: It was already mentioned that the photo-generated current from the pn-junction plays an important role in the shift of the measured Kelvin bias (Point 1). Annealing of the samples reduces the defect density in the implanted region and therefore the carrier lifetime is increased. This means in fact that more of the photo-generated electrons or holes will reach the Si surface, altering the surface potential.

4.4. Self-organized immobilization of biomolecules

4.4.1. DNA single strands

A potential application for the PolCarr substrates is their utilization in DNA microarrays. Exploiting the electrostatic forces for the immobilization of capture probes

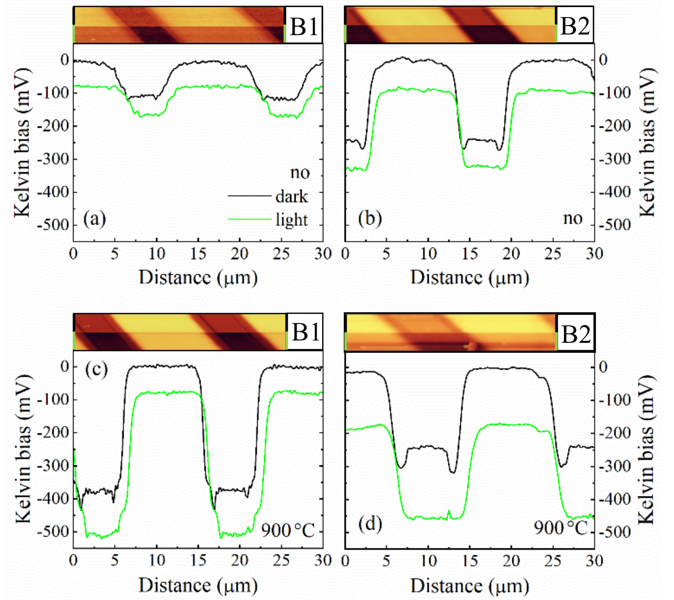

Figure 7: Influence of light illumination on the Kelvin bias of boron implanted Si:P samples. The line scans (black, without) and (green, with) illumination are taken from the 2D scans above the images.

(short single stranded DNA sequences) would be an attractive alternative to commonly applied surface chemistry. As a first step towards this goal we investigated phosphorus implanted PolCarr substrates and their interaction with a 30mer single stranded DNA oligonucleotide. In order to verify the self-organized immobilization of oligonucleotides on the substrates, we employed an enzyme catalyzed deposition of silver nanoparticles enabling a highly sensitive detection of the biotin labelled oligonucleotides. Due to the specific interaction of biotin and streptavidin, the silver nanoparticles are only deposited in those areas, where the biotin labelled molecules are located. Fig. 9 shows an implanted silicon substrate after modification with oligonucleotides and performing the enzyme catalyzed silver deposition. Apparently, the oligonucleotides are preferentially localized in the 10 µm wide areas between the 2 µm broad implanted stripes. This indicates that the negatively charged DNA molecules are attracted by the weakly positively charged areas between the phosphorus implanted stripes, which themselves feature a negative charge. This result suggests that the PolCarr substrates with a well defined SNEF pattern allow for a targeted immobilization of biomolecules such as single stranded DNA exploiting electrostatic interactions between biomolecules and the substrate surface.

4.4.2. Bovine serum albumin

Confocal microscopy images of the local BSA adsorption are shown in Fig. 10(a) for a sample of type B2 and (b) for sample of type P2. The BSA is in both cases adsorbed above B doped regions due to the attractive electrostatic force between the positive charged defect states at

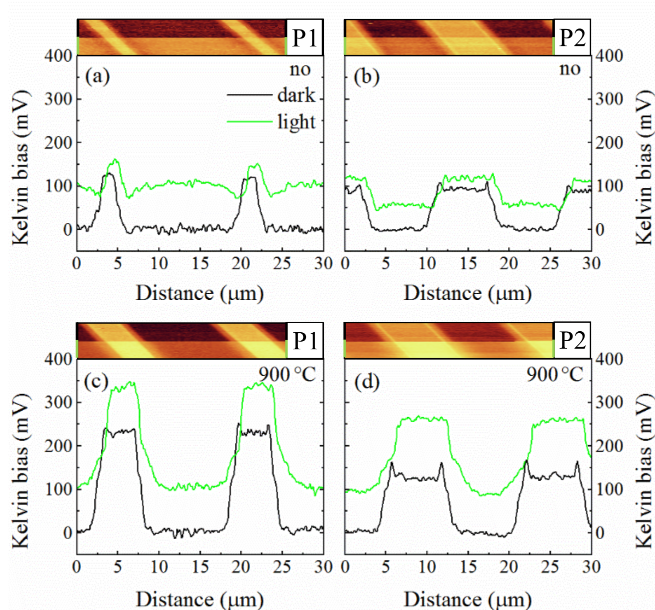

Figure 8: Influence of light illumination on the Kelvin bias of phosphorus implanted Si:B samples. The line scans (black, without) and (green, with) illumination are taken from the 2D scans above the images.

the SiO_2/Si interface and the BSA, which was negatively charged during incubation in PBS with pH 7.4 (isoelectric point BSA 4.7) [31].

5. Conclusions and Outlook

$1\times1\,cm^2$ large pieces of four different bulk-functionalized, planar Si substrates (P1, P2, B1, B2) with stripe-patterned surface-near electrostatic forces (SNEF) were fabricated by local ion implantation of phosphorus or boron ions into a 4 inch boron doped silicon wafer (Si:B) or phosphorus doped silicon wafer (Si:P), respectively. Without further treatment a 1–2 nm thin native SiO_2 layer forms on the Si surface and positive and negative interface charges with an areal density of up to $10^{12}\,cm^{-2}$ are immobilized at the interface between native SiO_2 and phosphorus implanted/doped silicon and boron implanted/doped silicon, respectively. The SNEF have been characterized using KPFM measurements in a $30 \times 30\,\mu m^2$ scan range with few nanometer resolution. First and second harmonics of the SNEF have been measured without and under illumination. The position dependent variation of the measured Kelvin signal which has been derived from 1st harmonics of the surface-near electrostatic forces has been modelled using the BHS model and the CPD model corrected by surface and interface charges. The measured Kelvin signal is always smaller for silicon with boron dopants (Si:B) in comparison to silicon with phosphoros dopants (Si:P). Under illumination the Kelvin signal is increased and decreased for boron doped host wafers (Si:B) and for phosphorus doped host wafers (Si:P), respectively. In addition,

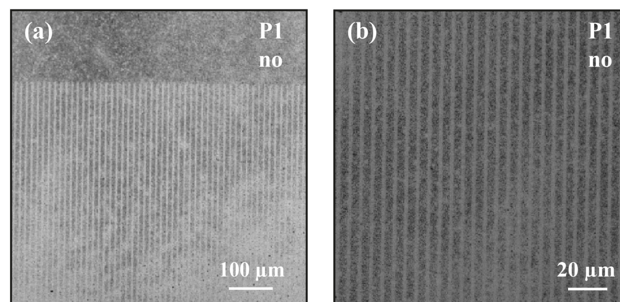

Figure 9: Optical microscopy images of (a,b) a phosphorus implanted silicon substrate (P1, no annealing) after self-organized immobilization of oligonucleotides under day-light conditions and after the enzyme catalyzed silver deposition indicated by dark areas. (a) The zoom-out optical microscopy image shows that the biotin modified oligonucleotides being negatively charged were immobilized in non-implanted regions (Si:B) being positively charged. (b) Shows the zoom-in optical microscopy image of (a).

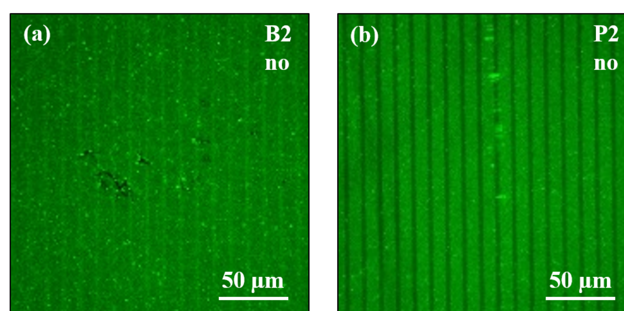

Figure 10: Confocal microscopy images of (a) a boron implanted silicon substrate (B2, no annealing) and of (b) a phosphorus implanted silicon substrate (P2, no annealing) after modification with fluorescence labeled BSA under day-light conditions. The areas with green fluorescence show that the negatively charged BSA is immobilized at boron doped regions.

the position of the pn-junction between implanted regions and non-implanted regions in the silicon host wafer can be recognized from an overshoot of measured Kelvin signal in the depletion regions of the pn-junction. The free carrier concentration has been derived from the 2nd harmonics of the surface-near electrostatic forces. They confirm larger concentration of free carriers in implanted regions in comparison to non-implanted regions of the silicon host wafer. The ability of the locally implanted silicon host wafers for a self-organized, local immobilization of charged analytes was successfully tested with single stranded DNA oligonucleotides and with BSA for future use as an electrochemical signal enhancer with high selectivity and as protein purifier with high efficiency, respectively. Mainly the interface charges in occupying the SiO_2/Si interface states of the non-implanted and implanted silicon host wafers acted on the charged analytes. We observed that the DNA was mainly immobilized on non-implanted regions of boron doped silicon wafers with positive interface charges and that the BSA was immobilized on the non-implanted re-

gions of phosphorus implanted boron doped silicon wafers and on the implanted regions of boron implanted phosphorus doped Si, both with positive interface charges.
In a future work, the formation of intrinsic acceptor-like and donor-like defects and resulting different types of interface charges and SNEF pattern will be investigated in silicon implanted silicon wafers, e.g. for potential use as silicon-based neuroimplants. In order to increase the areal concentration of immobile interface charges and corresponding local variation of SNEF, different ultrathin insulators on the Si substrates (SiON, SiN) will be investigated. Furthermore, masking of the SNEF by mobile surface charges which depend on the isoelectronic point of the ultrathin insulator will be controlled by matching the pH value of the solvent and the isoelectronic point of the ultrathin insulator when choosing the insulator material for a given pH value or when setting the pH value for a given insulator material.
In summary, presented planar silicon with patterned surface-near electrostatic forces allow for localized immobilization of charged analytes.

Acknowledgements

The authors thank H. Hilliges and G. Schnabel from HZDR for the preparation of the resist mask for ion implantation and Dr. D. Täuber from Leibniz-IPHT for initializing KPFM measurements under illumination. Furthermore, financial support from the Sächsische Aufbaubank (SAB-Project 100260515), Thüringer Aufbaubank (EFRE-OP 2014-2020), as well as the support by the Ion Beam Center (IBC) at HZDR, is gratefully acknowledged.

References

[1] N. Fischer, J. He, C. Aparicio, Surface immobilization chemistry of a laminin-derived peptide affects keratinocyte activity, Coatings 10 (2020) 560. doi:10.3390/coatings10060560.

[2] L. P. Kreuzer, M. J. Männel, J. Schubert, R. P. M. Höller, M. Chanana, Enzymatic catalysis at nanoscale: Enzyme-coated nanoparticles as colloidal biocatalysts for polymerization reactions, ACS Omega 2 (10) (2017) 7305–7312, pMID: 30023545. arXiv:https://doi.org/10.1021/acsomega.7b00700, doi:10.1021/acsomega.7b00700.
URL https://doi.org/10.1021/acsomega.7b00700

[3] W.-C. Chou, W.-P. Hu, Y.-S. Yang, H. W.-H. Chan, W.-Y. Chen, Neutralized chimeric dna probe for the improvement of gc-rich rna detection specificity on the nanowire field-effect transistor, Scientific Reports 9 (1) (2019) 11056–.
URL https://doi.org/10.1038/s41598-019-47522-9

[4] J. I. A. Rashid, N. A. Yusof, The strategies of dna immobilization and hybridization detection mechanism in the construction of electrochemical dna sensor: A review, Sensing and Bio-Sensing Research 16 (2017) 19 – 31. doi:https://doi.org/10.1016/j.sbsr.2017.09.001.
URL http://www.sciencedirect.com/science/article/pii/S2214180417300788

[5] H. Schmidt, S. Habicht, S. Feste, A.-D. Müller, O. G. Schmidt, Kelvin probe force microscopy for characterizing doped semiconductors for future sensor applications in nano- and biotechnology, Applied Surface Science 281 (2013) 24 – 29. doi:https://doi.org/10.1016/j.apsusc.2013.04.080.
URL http://www.sciencedirect.com/science/article/pii/S0169433213007848

[6] M. Nonnenmacher, M. P. O'Boyle, H. K. Wickramasinghe, Kelvin probe force microscopy, Applied Physics Letters 58 (25) (1991) 2921–2923. arXiv:https://doi.org/10.1063/1.105227, doi:10.1063/1.105227.
URL https://doi.org/10.1063/1.105227

[7] L. Kelvin, V. contact electricity of metals, Philos. Mag. 46 (278) (1898) 82–120. arXiv:https://doi.org/10.1080/14786449808621172, doi:10.1080/14786449808621172.
URL https://doi.org/10.1080/14786449808621172

[8] C. Baumgart, M. Helm, H. Schmidt, Quantitative dopant profiling in semiconductors: A Kelvin probe force microscopy model, Phys. Rev. B 80 (8) (2009) 085305. doi:10.1103/PhysRevB.80.085305.
URL https://link.aps.org/doi/10.1103/PhysRevB.80.085305

[9] C. Baumgart, A.-D. Müller, F. Müller, H. Schmidt, Kelvin probe force microscopy in the presence of intrinsic local electric fields, physica status solidi (a) 208 (4) (2011) 777–789. doi:10.1002/pssa.201026251.
URL http://dx.doi.org/10.1002/pssa.201026251

[10] R. Shikler, N. Fried, T. Meoded, Y. Rosenwaks, Measuring minority-carrier diffusion length using a kelvin probe force microscope, Phys. Rev. B 61 (2000) 11041–11046. doi:10.1103/PhysRevB.61.11041.
URL https://link.aps.org/doi/10.1103/PhysRevB.61.11041

[11] L. Polak, R. J. Wijngaarden, Two competing interpretations of kelvin probe force microscopy on semiconductors put to test, Phys. Rev. B 93 (2016) 195320. doi:10.1103/PhysRevB.93.195320.
URL https://link.aps.org/doi/10.1103/PhysRevB.93.195320

[12] J. Jo, J. Yoon, T. Lee, H.-Y. Cho, J.-Y. Lee, J.-W. Choi, H_2o_2 biosensor consisted of hemoglobin-dna conjugate on nanoporous gold thin film electrode with electrochemical signal enhancement, Nano Convergence 6 (1) (2019) 1–8.
URL https://doi.org/10.1186/s40580-018-0172-z

[13] X. Jia, X. Hu, W. Wang, C. Du, Non-covalent loading of ionic liquid-functionalized nanoparticles for bovine serum albumin: experiments and theoretical analysis, RSC Adv. 9 (2019) 19114–19120. doi:10.1039/C9RA02265A.
URL http://dx.doi.org/10.1039/C9RA02265A

[14] M. Yasuda, K. Ono, T. Nomura, S. H. Brewer, O. Halskau, S. Volden, W. R. Glomm, Bsa adsorption and immobilization onto charged monodisperse polymer nanoparticles, J Biosens Bioelectron 6 (2015) 000183. doi:10.4172/2155-6210.1000183.
URL http://dx.doi:10.4172/2155-6210.1000183

[15] J. F. Ziegler, J. P. Biersack, U. Littmark, The Stopping and Range of Ions in Solids, New York: Pergamon, 1985, www.srim.org.

[16] F. Müller, A.-D. Müller, Frequency dependent kelvin probe force microscopy on silicon surfaces, Journal of Vacuum Science & Technology B: Microelectronics and Nanometer Structures Processing, Measurement, and Phenomena 27 (2) (2009) 969–974. arXiv:https://avs.scitation.org/doi/pdf/10.1116/1.3039682, doi:10.1116/1.3039682.
URL https://avs.scitation.org/doi/abs/10.1116/1.3039682

[17] A. Kikukawa, S. Hosaka, R. Imura, Silicon pn junction imaging and characterizations using sensitivity enhanced kelvin probe force microscopy, Applied Physics Letters 66 (25) (1995) 3510–3512. arXiv:https://doi.org/10.1063/1.113780, doi:10.1063/1.113780.
URL https://doi.org/10.1063/1.113780

[18] A. K. Henning, T. Hochwitz, J. Slinkman, J. Never, S. Hoffmann, P. Kaszuba, C. Daghlian, Two-dimensional surface dopant profiling in silicon using scanning kelvin probe microscopy, Journal of Applied Physics 77 (5) (1995) 1888–

1896. arXiv:https://doi.org/10.1063/1.358819, doi:10.1063/1.358819.
URL https://doi.org/10.1063/1.358819

[19] W. Melitz, J. Shen, A. C. Kummel, S. Lee, Kelvin probe force microscopy and its application, Surface Science Reports 66 (1) (2011) 1 – 27. doi:https://doi.org/10.1016/j.surfrep.2010.10.001.
URL http://www.sciencedirect.com/science/article/pii/S0167572910000841

[20] L. Polak, R. J. Wijngaarden, Quantitative Analysis of Kelvin Probe Force Microscopy on Semiconductors, Springer International Publishing, Cham, 2018, pp. 227–247. doi:10.1007/978-3-319-75687-5_9.
URL https://doi.org/10.1007/978-3-319-75687-5_9

[21] B.-Y. Tsui, C.-M. Hsieh, P.-C. Su, S.-D. Tzeng, S. Gwo, Two-dimensional carrier profiling by kelvin-probe force microscopy, Japanese Journal of Applied Physics 47 (6) (2008) 4448–4453. doi:10.1143/jjap.47.4448.
URL https://doi.org/10.1143%2Fjjap.47.4448

[22] M. Grundmann, The Physics of Semiconductors: An Introduction Including Devices and Nanophysics, Springer-Verlag, 2006.

[23] E. Antoncik, On the lattice location of implanted impurities in silicon, Nuclear Instruments and Methods in Physics Research Section B: Beam Interactions with Materials and Atoms 14 (2) (1986) 193 – 203. doi:https://doi.org/10.1016/0168-583X(86)90044-3.
URL http://www.sciencedirect.com/science/article/pii/0168583X86900443

[24] W. F. J. Frank, B. S. Berry, Lattice location and atomic mobility of implanted boron in silicon, Radiation Effects 21 (2) (1974) 105–111. arXiv:https://doi.org/10.1080/10420157408230818, doi:10.1080/10420157408230818.
URL https://doi.org/10.1080/10420157408230818

[25] N. P. Dikiy, P. P. Matyash, P. A. Svetashev, N. A. Skakun, V. K. Vasilev, E. I. Zorin, P. V. Pavlov, D. U. Tetelbaum, Lattice location of phosphorus atoms implanted into silicon, physica status solidi (a) 32 (2) (1975) K165–K167. arXiv:https://onlinelibrary.wiley.com/doi/pdf/10.1002/pssa.\-2210320264, doi:10.1002/pssa.2210320264.
URL https://onlinelibrary.wiley.com/doi/abs/10.1002/pssa.\discretionary{-}{}{}2210320264

[26] M. Vos, D. Boerma, P. Smulders, S. Oosterhoff, Defect and dopant depth profiles in boron-implanted silicon studied with channeling and nuclear reaction analysis, Nuclear Instruments and Methods in Physics Research Section B: Beam Interactions with Materials and Atoms 17 (3) (1986) 234 – 241. doi:https://doi.org/10.1016/0168-583X(86)90062-5.
URL http://www.sciencedirect.com/science/article/pii/0168583X86900625

[27] S. Hasegawa, H. Ishiwara, S. Furukawa, T. Shimizu, The lattice location of phosphorus atoms implanted into silicon, Japanese Journal of Applied Physics 15 (2) (1976) 391.
URL http://stacks.iop.org/1347-4065/15/i=2/a=391

[28] M. Jadan, A. R. Chelyadinskii, V. Y. Yavid, Displacement of boron from the silicon crystal nodes by interstitial si atoms during implantation and annealing, American Journal of Applied Sciences 2 (2005) 910–913.

[29] D. K. Schroder, Surface voltage and surface photovoltage: history, theory and applications, Measurement Science and Technology 12 (3) (2001) R16–R31. doi:10.1088/0957-0233/12/3/202.
URL https://doi.org/10.1088%2F0957-0233%2F12%2F3%2F202

[30] L. Kronik, Y. Shapira, Surface photovoltage spectroscopy of semiconductor structures: at the crossroads of physics, chemistry and electrical engineering, Surface and Interface Analysis 31 (10) (2001) 954–965. arXiv:https://onlinelibrary.wiley.com/doi/pdf/10.1002/sia.1132, doi:10.1002/sia.1132.
URL https://onlinelibrary.wiley.com/doi/abs/10.1002/sia.1132

[31] A. Salis, M. Boström, L. Medda, F. Cugia, B. Barse, D. F. Parsons, B. W. Ninham, M. Monduzzi, Measurements and theoretical interpretation of points of zero charge/potential of bsa protein, Langmuir 27 (18) (2011) 11597–11604, pMID: 21834579. arXiv:https://doi.org/10.1021/la2024605, doi:10.1021/la2024605.
URL https://doi.org/10.1021/la2024605